

# Conformational plasticity of the intracellular cavity of GPCR–G-protein complexes leads to G-protein promiscuity and selectivity

Manbir Sandhu<sup>a,b</sup>, Anja M. Touma<sup>c</sup>, Matthew Dysthe<sup>c</sup>, Fredrik Sadler<sup>c</sup>, Sivaraj Sivaramakrishnan<sup>c,1</sup>, and Nagarajan Vaidehi<sup>a,b,1</sup>

<sup>a</sup>Irell & Manella Graduate School of Biological Sciences, Beckman Research Institute of the City of Hope, Duarte, CA 91010; <sup>b</sup>Department of Computational & Quantitative Medicine, Beckman Research Institute of the City of Hope, Duarte, CA 91010; and <sup>c</sup>Department of Genetics, Cell Biology, and Development, University of Minnesota, Twin Cities, Minneapolis, MN 55455

Edited by Robert J. Lefkowitz, Howard Hughes Medical Institute, Duke University Medical Center, Durham, NC, and approved May 2, 2019 (received for review December 13, 2018)

While the dynamics of the intracellular surface in agonist-stimulated GPCRs is well studied, the impact of GPCR dynamics on G-protein selectivity remains unclear. Here, we combine molecular dynamics simulations with live-cell FRET and secondary messenger measurements, for 21 GPCR–G-protein combinations, to advance a dynamic model of the GPCR–G-protein interface. Our data show C terminus peptides of  $G_{\alpha_s}$ ,  $G_{\alpha_i}$ , and  $G_{\alpha_q}$  proteins assume a small ensemble of unique orientations when coupled to their cognate GPCRs, similar to the variations observed in 3D structures of GPCR–G-protein complexes. The noncognate G proteins interface with latent intracellular GPCR cavities but dissociate due to weak and unstable interactions. Three predicted mutations in  $\beta_2$ -adrenergic receptor stabilize binding of noncognate  $G_{\alpha_q}$  protein in its latent cavity, allowing promiscuous signaling through both  $G_{\alpha_s}$  and  $G_{\alpha_q}$  in a dose-dependent manner. This demonstrates that latent GPCR cavities can be evolved, by design or nature, to tune G-protein selectivity, giving insights to pluridimensional GPCR signaling.

G-protein–coupled receptor | GPCR | functional selectivity | structural plasticity | dynamics

**G**-protein–coupled receptors (GPCRs) bind a diverse array of agonists and regulate multiple physiological processes. Upon binding agonists, GPCRs couple to single or multiple G-protein subtypes and initiate cell-specific signaling pathways. Studies with novel bioluminescence resonance energy transfer sensors show GPCRs exhibit a promiscuous and “pluridimensional” behavior, coupling to many  $G_{\alpha}$ -proteins with different strengths (1–4). While a receptor may show similar affinity to different  $G_{\alpha}$  proteins, the cellular context may render certain couplings moot (1, 5–9). There are four major subtypes of heterotrimeric ( $G_{\alpha\beta\gamma}$ ) G proteins, typified by the  $G_{\alpha}$  subunit:  $G_{\alpha_s}$ ,  $G_{\alpha_i}$ ,  $G_{\alpha_q/11}$ , and  $G_{\alpha_{12/13}}$ . The downstream cellular response elicited by G-protein signaling pathways are dependent on these distinct  $G_{\alpha}$ -protein subfamilies. Current models of G-protein signaling cannot explain why certain GPCRs bind multiple subtypes, while others are selective. Currently, seven distinct 3D structures of Class A agonist–GPCR–G-protein complexes (10–16) provide details on the residue interactions in the GPCR–G-protein interface. This structural information, coupled with phylogenetic analysis of GPCR and G-protein sequences, highlight the G-protein barcodes for selectivity (17, 18). However, untangling which of these interacting pairs are critical “hotspots” mediating selectivity warrants probing the dynamics of the GPCR–G-protein interface, the focus of our current study.

Seminal works have shed light on the critical involvement of GPCR intracellular (IC) loops and the transmembrane (TM) helix 6 (TM6) interface in mediating selective G-protein interactions (19–23). Analysis of 3D structures combined with previous cell-based assay studies show the  $\alpha 5$  helix in the C terminus of the  $G_{\alpha}$  protein exhibits a large effect on selective coupling to

GPCRs (24–29). Here we study the dynamic interactions of the C terminus of  $G_{\alpha_s}$ ,  $G_{\alpha_i}$ , and  $G_{\alpha_q}$  proteins, hereafter referred to as s-pep, i-pep, and q-pep, in combination with seven class A GPCRs ( $\beta_2$ -Adrenergic Receptor,  $\beta_2$ AR;  $\beta_3$ -Adrenergic Receptor,  $\beta_3$ AR; Dopamine 1 Receptor,  $D_1$ R;  $\alpha_2$ A-Adrenergic Receptor,  $\alpha_2$ AR; Cannabinoid 1 Receptor,  $CB_1$ R;  $\alpha_1$ A-Adrenergic Receptor,  $\alpha_1$ AR; and Vasopressin 1A Receptor,  $V_{1A}$ R), to delineate the GPCR–G-protein selectivity determinants. Our focus is to delineate the contribution of the receptor–G-protein dynamics in G-protein selectivity and promiscuity.

Previous receptor dynamics studies showed that agonist binding makes the IC half of the receptor more dynamic and conformationally heterogeneous (30–32), while G-protein binding stabilizes the GPCR conformation and increases the affinity of a GPCR for a full agonist (33–35). Detailed dynamics studies of the agonist–GPCR– $G_{\alpha}$ -protein complex to identify selectivity determinants are sparse. In this work, we use extensive Molecular Dynamics (MD) simulations combined with a scalable fluorescence resonance energy transfer (FRET) sensor technique called Systematic Protein Affinity Strength Modulation (SPASM) that is performed in live cells. The advantage of the SPASM technique is

## Significance

Structures of GPCR–G-protein complexes show how cognate G proteins interact with GPCRs. However, noncognate GPCR–G-protein interactions are poorly understood, despite their relevance in cells. The conceptual advancements in our study show 1) the C terminus of  $G_{\alpha_s}$ ,  $G_{\alpha_i}$ , and  $G_{\alpha_q}$  proteins assume a small dynamic ensemble of unique orientations when coupled to their cognate GPCRs, explaining the variations observed in the X-ray and cryo-EM structures of GPCR–G-protein complexes; and 2) the noncognate G proteins interact dynamically with latent, previously uncharacterized cavities within the GPCR cytosolic cavity. Engineering these latent cavities with hotspots to the noncognate G proteins tunes promiscuity in the GPCR. This study provides a framework for understanding how GPCR dynamics subtly modulate signaling in different pathways.

Author contributions: M.S., S.S., and N.V. designed research; M.S., A.M.T., M.D., and F.S. performed research; M.S., A.M.T., S.S., and N.V. analyzed data; and M.S. and N.V. wrote the paper.

The authors declare no conflict of interest.

This article is a PNAS Direct Submission.

Published under the PNAS license.

<sup>1</sup>To whom correspondence may be addressed. Email: sivaraj@umn.edu or nvaidehi@cuh.org.

This article contains supporting information online at [www.pnas.org/lookup/suppl/doi:10.1073/pnas.1820944116/-DCSupplemental](http://www.pnas.org/lookup/suppl/doi:10.1073/pnas.1820944116/-DCSupplemental).

Published online May 28, 2019.

that tethering GPCRs to  $G\alpha$  proteins with the length-adjustable  $\alpha$ -helical ER/K linker (36) allows scaling of the effective localized concentration of GPCR and  $G\alpha$  protein to span various, plausible, cellular concentrations. SPASM is sensitive to measuring weak and dynamic protein–protein interactions in cellular conditions (29, 37, 38). This permits comparison between the binding affinities of cognate (canonical signaling partners) and noncognate (weak or uncharacterized partners)  $G\alpha$  proteins at the same stoichiometric ratios with the GPCR, which is not feasible with other biophysical techniques used in live cells (1, 4, 39, 40). Recent findings with SPASM FRET sensors show a physiologic effect of noncognate G proteins to prime GPCR signaling within the cell (41), demonstrating the importance for probing these noncognate G-protein interactions within the cell.

The key findings from our study are as follows: 1) The  $G\alpha$  peptides assume a small ensemble of unique orientations when coupled to a cognate GPCR. 2) The s-sep binds in a different IC cavity of its cognate GPCR and orients its C terminus toward TM helices 5 and 6 (TM5 and TM6) compared with i-pep and q-pep that orient toward TM2 and IC loop 1 (ICL1). 3) MD simulations of  $\beta_2$ AR complexed with the noncognate q-pep reveal formation of a transient cavity in the  $\beta_2$ AR IC interface, resembling the stable IC cavity observed in the  $V_{1A}$ R:q-pep complex. Mutation of the hotspot residues identified for  $G\alpha_q$  coupling in  $V_{1A}$ R, into  $\beta_2$ AR, stabilizes this transient cavity. We have generated a triple mutant,  $\beta_2$ AR–Q142K<sup>5,67</sup>–R228I<sup>5,68</sup>–Q229W<sup>34,54</sup>, that displays dose-dependent, isoproterenol-induced, promiscuity toward  $G\alpha_s$ - and  $G\alpha_q$ -coupled signaling pathways. 4) This promiscuous  $\beta_2$ AR mutant demonstrates that GPCRs contain defined, latent IC receptor cavities showing weak interactions with noncognate G proteins. These latent cavities can couple to the noncognate G proteins if stabilized with the necessary hotspot residues, through mutagenesis or natural evolution. The promiscuous  $\beta_2$ AR mutant thus serves as a model system to probe the dynamics of GPCRs exhibiting pluridimensional G-protein coupling. Our dynamics-based framework reveals the structural plasticity of the GPCR cytosolic pocket that underlies G-protein selectivity and the role of noncognate G-protein interactions in influencing GPCR dynamics. Furthermore, this study provides features of the GPCR–G-protein interaction that can be targeted by functionally selective drugs to tune therapeutic response to specific GPCR signaling pathways (42).

## Results

**Cognate GPCR– $G\alpha$ -Protein C Terminus Complexes Reveal Distinct Conformations for  $G\alpha_s$ ,  $G\alpha_i$ , and  $G\alpha_q$  Signaling Pairs.** We performed atomistic MD simulations and generated a minimum of 1- $\mu$ s ensembles for seven different class A GPCRs bound to full agonists and complexed with each of three  $G\alpha$  peptides (*SI Appendix, Table S1*). From the MD data, we detect that s-pep, i-pep, and q-pep insert in distinct cavities within the IC interface of their respective cognate GPCRs (Fig. 1 *A* and *B* and *SI Appendix, Fig. S1B*). The N terminus of the  $G\alpha$  peptides, which protrude out of the GPCR IC cavity, are highly flexible during the MD simulations and normally engaged in intramolecular interactions with the “Ras” domain of the  $G\alpha$  protein (43, 44). Therefore, we omitted the N-terminal region for analysis of receptor–G-protein contacts. The C terminus of the  $G\alpha$  peptides (indicated by “\*”, Fig. 1*B*) insert into the GPCR IC cavity and retain helicity. We have used the axis defined by this helical region of the  $G\alpha$  peptide [Common G-protein Numbering, residues H5.12 to H5.26 (17)] for our analyses of  $G\alpha$ -peptide orientation.

The GPCR conformations shown (Fig. 1*A* and *SI Appendix, Fig. S1B*) are the centroid of the most populated conformation cluster from the ensemble of MD trajectories with the cognate  $G\alpha$  peptide bound. The  $G\alpha$ -peptide conformations shown in Fig. 1*B*, are centroids from the top three populated clusters of

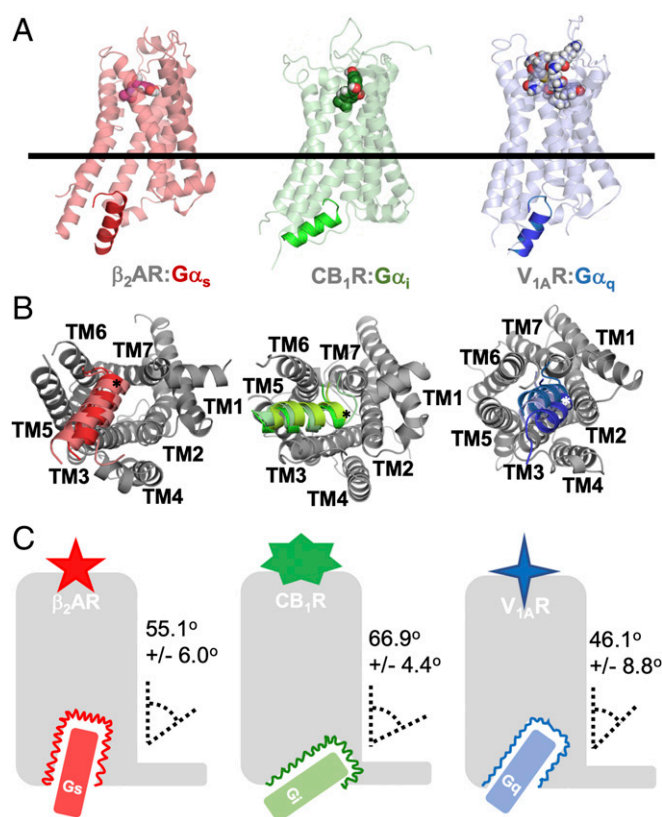


**Fig. 1.** The s-pep, i-pep, and q-pep reveal distinct binding orientations in GPCR cavity of respective, cognate GPCRs. (*A*) View of the  $\beta_2$ AR:s-pep (*Left*), CB<sub>1</sub>R:i-pep (*Center*), and V<sub>1A</sub>R:q-pep (*Right*) complexes. Each receptor is shown oriented parallel to the membrane-normal, with a horizontal plane bisecting the TM helices at the vertical center of the protein complex. The orientations of the three bound peptides in their respective cognate receptors vary. (*B*) IC view of each complex from *A*. Simulations were clustered by RMSD of the peptide backbone, and the representative conformation of the  $G\alpha$  peptide from the top three clusters is shown for each complex. In this view, we observe distinct differences with the orientation of each peptide, particularly that the C-terminal end of the helical portion of each peptide (denoted by “\*”) points toward distinct IC regions of the respective GPCRs. (*C*) A schematic for each unique GPCR– $G\alpha$ -peptide complex is shown. The colored wavy line which outlines the receptor IC cavity surrounding the  $G\alpha$  peptide represents the dynamic interface of the GPCR as it contacts and interfaces the G-protein C terminus. We have calculated the insertion angle of the principle axis of the G-protein C terminus with the principle axis of the GPCR and provided this value here. See also *SI Appendix, Fig. S1*.

these simulations. The central region of all of the three  $G\alpha$  peptides are anchored to TM5 and ICL2 of their given GPCRs. The extreme C termini of i-pep and q-pep orient toward TM2, ICL1, and ICL2 in their cognate GPCRs, while the C terminus of s-pep orients toward an interface between TM6 and TM7 (Fig. 1*B* and *SI Appendix, Fig. S1B*). We calculated the insertion of the  $G\alpha$  peptides in their cognate GPCRs as the angle between the principal axis of the GPCR TM core bundle and principal axis of the  $G\alpha$ -protein  $\alpha 5$  helix for each cognate GPCR–G-protein simulation. We did the same for the X-ray and cryo-Electron Microscopy (cryo-EM) structures (Fig. 1*C* and *SI Appendix, Fig. S1B* and *Table S2*). The three  $G\alpha$ -protein subtypes show different angles of insertion in the GPCR IC cavity. There is also variation in the insertion angles even among the three  $G\alpha_s$  coupled receptors studied here. Our previous FRET sensor studies (29, 37) have shown differences in coupling strengths of  $G\alpha_s$  to  $\beta_2$ AR,  $\beta_3$ AR, and D<sub>1</sub>R in the order  $\beta_2$ AR >  $\beta_3$ AR > D<sub>1</sub>R. As shown in *SI Appendix, Fig. S1C*,



the calculated average interaction energy from MD simulations of s-pep with  $\beta_2$ AR,  $\beta_3$ AR, and  $D_1$ R showed the same trend as observed in the FRET sensor experiments. We

speculate that the differences in the  $\alpha 5$ -helix insertion may modulate the strength of interaction between GPCR and  $G\alpha$  peptide.

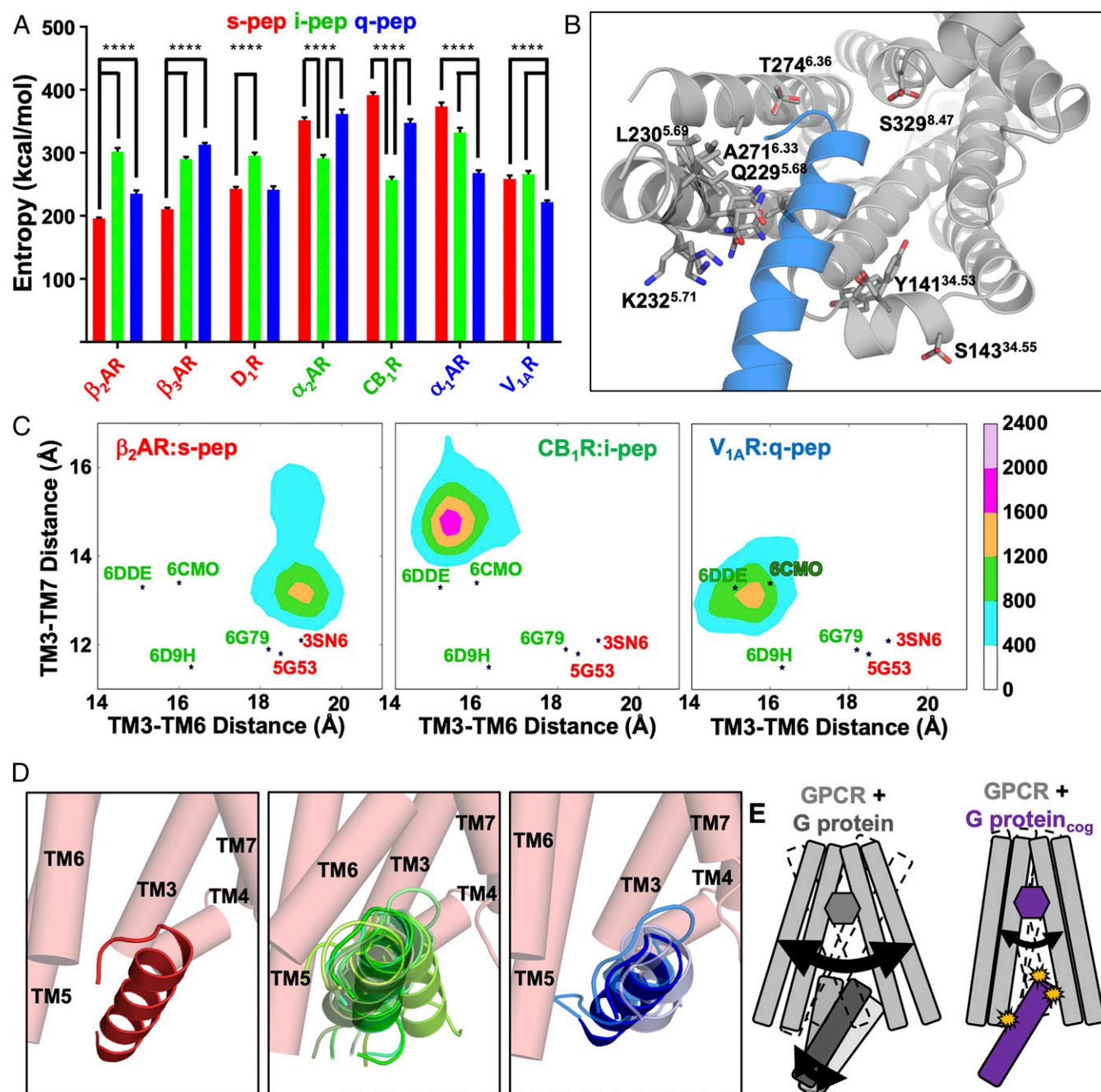


**Fig. 2.** Dynamic properties of the cognate and noncognate agonist-GPCR- $G\alpha$ -peptide interfaces that stabilize a signaling complex. (A) First-order torsional entropy values calculated at 300 K, using torsion angles distribution for the GPI residues of each GPCR in the presence of cognate and noncognate  $G\alpha$  peptides. Values are shown as means from five replicate simulations  $\pm$  SEM for s-pep (red), i-pep (green), and q-pep (blue). Significance was calculated using two-sided ANOVA; \*\*\*\* $P < 0.0001$ . (B) Visual model of the sampled rotamer conformations for the GPI residues of the  $\beta_2$ AR with the highest entropy values when bound to noncognate  $G\alpha$  peptides. The spread of sampled rotamer angles is shown in transparent sticks. (C) Population distribution of the MD simulation snapshots for  $\beta_2$ AR,  $CB_1$ R, and  $V_{1A}$ R when bound to their respective agonists and cognate  $G\alpha$  peptides, with respect to interresidue distances between TM3 and TM6, and TM3 and TM7, shown in *SI Appendix, Fig. S2A*; "\*" denotes the interresidues distances for X-ray and cryo-EM structures, colored as in A, based on G-protein preference: 3SN6- $G\alpha_s$ -bound  $\beta_2$ AR (red); 5G53-mini- $G\alpha_s$ -bound  $A_2$ AR (red); 6DDE- $G\alpha_i$ -bound  $\mu$ OR (green); 6D9H- $G\alpha_i$ -bound  $A_1$ R (green); 6G79- $G\alpha_o$ -bound 5HT-1BR (green); and 6CMO- $G\alpha_i$ -bound Rhodopsin (green). (D) Representation of centroids from conformational clusters of the cognate and noncognate  $G\alpha$  peptides bound to  $\beta_2$ AR (shown as pink cylinders). The top clusters making up 85% of the conformational ensemble are shown. The noncognate i-pep (nine clusters, green) and q-pep (three clusters, blue) in  $\beta_2$ AR show greater flexibility as multiple conformation clusters compared with s-pep (one cluster, red). (E) Model derived from the data in this figure: Both receptor and (cognate and noncognate)  $G\alpha$  peptides are highly dynamic upon interaction (Left). Thermodynamically favorable interactions allow the GPCR IC cavity to clamp onto the  $G\alpha$  peptide and stabilize the dynamics of the complex (Right). See also *SI Appendix, Fig. S2*.

**Only Cognate GPCR–Gα-Peptide Pairs Stabilize Clamping of GPCR IC Cavity on α5 Helix.** GPCRs and G proteins cluster in plasma membrane domains (45), inflating the relative concentration of cognate and noncognate G proteins compared with GPCRs (5). Gupte et al. (41) showed that noncognate G proteins can synergize the signaling efficacy of cognate G proteins. To assess how cognate and noncognate G-protein interactions affect the GPCR IC cavity, we calculated the first-order torsional entropy of the GPCR residues which interface the G protein (GPI) (Fig. 2*A* and *SI Appendix, Table S4*). A schematic of side-chain conformations of the β<sub>2</sub>AR residues with highest entropy is shown (Fig. 2*B*). The GPI residues show lower entropy when coupled to their cognate G proteins compared with noncognate G proteins. We also observed increased flexibility in the GPCR IC cavity measured as the distance between residues 3.50 and 6.30 (*SI Appendix, Fig. S24*) (46) when bound to noncognate G proteins (*SI Appendix, Fig. S2B* and *Table S3*). The residue notations shown are the Ballesteros–Weinstein GPCR numbering system (47). The reduced entropy and flexibility of cognate interactions allows the GPCR residues in the IC cavity to form strong enthalpic interactions with the G protein, except in the Gα<sub>q</sub>-coupled α<sub>1A</sub>AR. We and others have shown, through live-cell coupling data, that α<sub>1A</sub>AR interacts promiscuously with all three Gα peptides (29, 48).

The elongation of the interresidue distance between residues 3.50 and 6.30 and the contraction of the residue distance between 3.50 and 7.53 are characteristics of GPCR activation (46, 49, 50) (*SI Appendix, Fig. S24*). MD trajectories of β<sub>2</sub>AR, β<sub>3</sub>AR, and D<sub>1</sub>R complexed with s-pep projected on these two distances show ensembles of states close to the conformation in the crystal structure of β<sub>2</sub>AR with nucleotide-free Gs [Protein Data Bank (PDB) ID code 3SN6] and adenosine 2A Receptor (A<sub>2A</sub>R) bound to mini-Gs protein (PDB ID code 5G53; Fig. 2*C* and *SI Appendix, Fig. S2C*). Both CB<sub>1</sub>R and V<sub>1A</sub>R, with i-pep and q-pep, respectively (Fig. 2*C*), show ensembles representing the active state identified in the cryo-EM structures of μ Opioid Receptor (μOR) and Rhodopsin with nucleotide-free trimeric Gi (PDB ID codes 6DDE and 6CMO). We also observe that the α<sub>2A</sub>AR and α<sub>1A</sub>AR both sample active states similar to the A<sub>2A</sub>R bound to mini-Gs, Serotonin 1B Receptor (5HT-1B) bound Go protein, and β<sub>2</sub>AR bound to nucleotide-free Gα<sub>s</sub> (PDB ID codes 5G53, 6G79, and 3SN6). These distances in the X-ray and cryo-EM structures of G-protein-bound class A GPCRs are also shown in *SI Appendix, Table S2*.

We analyzed the Gα-peptide conformational dynamics by clustering the Gα-peptide MD simulation trajectories using root-mean-square deviation (RMSD) in coordinates. The cognate Gα peptide is stabilized in the majority of the seven GPCRs, revealed by fewer conformational clusters compared with the number of clusters sampled by noncognate Gα peptides (*SI Appendix, Table S5*). In the cognate interaction of β<sub>2</sub>AR with the s-pep, >85% of the MD snapshots are located within the top cluster (Fig. 2*D, Left*), whereas the noncognate i-pep (green) and q-pep (blue) sample only 30% (top nine clusters to reach >85% population) and 67% (top three clusters to reach >85% population), respectively, of the population within the top cluster (Fig. 2*D, Center and Right*). Taken together, these results show that the GPCR clamps tighter on the cognate Gα C terminus, lowering the flexibility, and improves the enthalpic interaction leading to productive signaling (Fig. 2*E*). The noncognate Gα peptides show high flexibility, show weaker interactions in the GPCR IC cavity, and eventually fall out of the cavity.

**Identifying Amino Acid Hotspots in the C Terminus α5 Helix That Confer Selectivity to GPCRs.** We used an iterative combination of MD simulation analysis and SPASM experiments to identify the amino acid residues in each Gα peptide which confer selectivity to their cognate receptors among the seven studied (*SI Appendix, Fig. S3*). We identified residues on the Gα peptide that remain in

helical conformation, and show above-average favorable interaction energies and sustained contacts (with >50% frequency) during the dynamics with the GPCR (shown in yellow boxes and bold, colored font, Fig. 3*A* and *Materials and Methods*). We observe these predicted selectivity hotspot residues to be both conserved and mutated across the Gα peptides. Where applicable, the hotspot residues were swapped with homologous positions from another Gα peptide, and binding was tested with the cognate GPCRs for both the cognate and mutated noncognate Gα peptides. For the hotspots conserved in both position and sequence across Gα peptides, the residue was mutated to alter amino acid physical characteristics and test disruption in the cognate complex.

We hypothesized that the swapping mutations would enable GPCRs to couple to noncognate Gα peptides with appropriate “cognate-like” swapping mutations. We tested this swapping between s-pep and q-pep and also between i-pep and q-pep using β<sub>2</sub>AR for Gα<sub>s</sub> coupling, V<sub>1A</sub>R for Gα<sub>q</sub> coupling, and CB<sub>1</sub>R for Gα<sub>i</sub> coupling. The mutations were made in SPASM FRET sensor constructs and transiently transfected into HEK-293T cells. FRET ratio is measured as agonist-stimulated minus unstimulated FRET, and comparisons to the wild type (WT) were calculated (*SI Appendix, Table S6*). The swapping mutations in the cognate Gα peptides led to significant reduction in FRET intensity changes upon treatment with agonist as shown in Fig. 3*B, i* for β<sub>2</sub>AR with the q-like mutations in s-pep, Fig. 3*B, iii* for V<sub>1A</sub>R with s-like mutations in q-pep, Fig. 3*B, vii* for CB<sub>1</sub>R with q-like mutations in the i-pep, and Fig. 3*B, v* for V<sub>1A</sub>R with i-like mutations in q-pep. These results affirm the conclusion that Gα<sub>s</sub> residue E392<sup>H5.24</sup>, Gα<sub>q</sub> residues L349<sup>H5.16</sup>, E355<sup>H5.22</sup>, and N357<sup>H5.24</sup>, and Gα<sub>i</sub> residue G352<sup>H5.24</sup> are some of the selectivity hotspot residues. The details of the FRET data are discussed in *SI Appendix, Table S6*.

We performed reciprocal, gain-of-coupling experiments by introducing cognate hotspot residue mutations into homologous structural positions in noncognate Gα peptides. We performed FRET assays for β<sub>2</sub>AR with s-like mutations in q-pep (Fig. 3*B, ii*), V<sub>1A</sub>R with q-like mutations in s-pep and also q-like mutations in i-pep (Fig. 3*B, iv and vi*), and CB<sub>1</sub>R with i-like mutations in q-pep (Fig. 3*B, viii*). These data show that the following residue positions mediate significant increase in G protein coupling to the noncognate GPCR: Gα<sub>q</sub> residues E355Q<sup>H5.22</sup>, E355Q<sup>H5.22</sup>/L349Q<sup>H5.16</sup> with β<sub>2</sub>AR (Fig. 3*B, ii*); Gα<sub>s</sub> residues Q384L<sup>H5.16</sup>, E392N<sup>H5.24</sup> (Fig. 3*B, iv*), and Gα<sub>i</sub> residue T340K<sup>H5.12</sup> with V<sub>1A</sub>R (Fig. 3*B, vi*); and Gα<sub>q</sub> residues Q350K<sup>H5.17</sup>, N357G<sup>H5.24</sup> with CB<sub>1</sub>R (Fig. 3*B, viii*). Taken together, these results show that positions H5.16, H5.22, and H5.24 play a critical role in binding of all three Gα subtypes to their respective GPCRs, with positions H5.12 and H5.17 involved in ancillary roles within the Gα<sub>i</sub> and Gα<sub>q</sub> interactions. These experiments suggest that the IC cavity of a given GPCR recognizes a small number of critical structural features in the α5 helix of the Gα protein, and, if these minimal features are present in the correct orientation, the Gα protein can complex with the GPCR. This is exemplified in MD simulations of the β<sub>2</sub>AR with the noncognate q-pep becoming stabilized in the GPCR IC cavity, similar to the cognate s-pep, with the addition of the s-pep H5.16 and H5.22 hotspots (L349Q/E355Q) (*Movie S1*).

**Rational Design of a Promiscuous β<sub>2</sub>AR Gα<sub>q</sub>- and Gα<sub>s</sub>-Coupled Receptor.** Fig. 4*A* shows the contribution from residues in each TM and ICL region in the Gα<sub>s</sub>-, Gα<sub>i</sub>-, or Gα<sub>q</sub>-coupled receptors toward binding their cognate Gα peptides. The relative sizes of the circles reflect the percentage of total contacts (*SI Appendix, Table S7*) contributed from the TM or ICL region of the given GPCR. Specifically, Gα<sub>s</sub>-coupled receptors interact with the s-pep primarily through contacts on TM3, TM5, and TM6. The i-pep contacts the residues in TM3, TM5, TM6, and ICL2 in the Gα<sub>i</sub>-coupled receptors. Most contacts in Gα<sub>q</sub>-coupled receptors are from

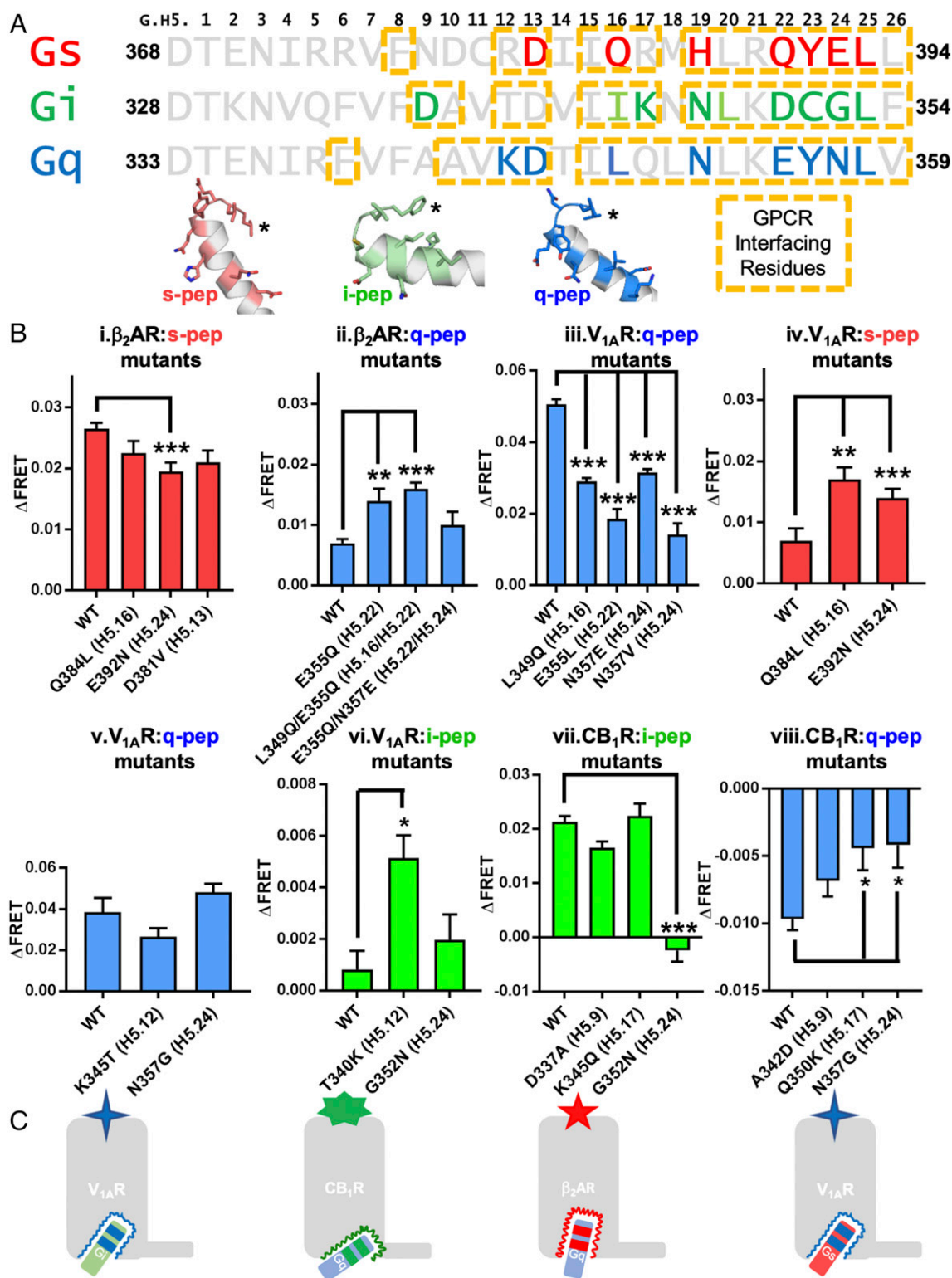


**Fig. 3.** Hotspots in the G-protein  $\alpha 5$  helix identified in cognate GPCR–G $\alpha$ -peptide pairs. (A) Sequence alignment of the  $\alpha 5$  helix of G $\alpha_s$ , G $\alpha_i$ , and G $\alpha_q$  C termini. The residues on the G $\alpha$  peptides that make up the GPCR-interfacing residues (based on frequency of interaction) with their cognate receptors are shown in yellow boxes. The significant energetically favorable residue hotspots are marked in bold and colored font in the respective sequences and shown in stick representation in the cartoon of the G $\alpha$  peptides shown below the alignment. The C termini of the peptides are marked with an asterisk for visual orientation. (B) Selectivity “hotspot” residues predicted from MD simulations were validated in SPASM FRET sensors, by mutating the G $\alpha$ -peptide residue to a homologous residue of another G $\alpha$  protein, and testing the interaction of the mutant G $\alpha$  peptide with the original cognate GPCR (i, iii, v, vii) or the cognate GPCR of the homologous “donor” G $\alpha$  peptide (ii, iv, vi, viii). (B, iv) Republished with permission of American Society for Biochemistry and Molecular Biology, from ref. 29; permission conveyed through Copyright Clearance Center, Inc. Mean FRET values were compared by one-way ANOVA and Tukey’s comparison of means. Significance is denoted as \* $P < 0.05$ , \*\* $P < 0.01$ , \*\*\* $P < 0.001$ . (C) The schematic model depicts that mutations to the selectivity hotspots in the  $\alpha 5$  helix orient noncognate G $\alpha$  peptides into a cognate-like orientation within a given GPCR, by making the G $\alpha$  peptide amenable to the GPCR cavity available for binding. See also *SI Appendix, Figs. S3 and S4*.



TM2, TM3, TM5, TM6, and ICL2. Both  $G_{\alpha_i}$ - and  $G_{\alpha_q}$ -coupled receptors, but not  $G_{\alpha_s}$ -coupled receptors, contact the C terminus of their respective peptides through ICL1 residues. The predicted pairwise interactions between the  $G_{\alpha}$  peptides and their respective cognate GPCRs are given in *SI Appendix, Table S8*.

Similar to the swapping mutations we tested in  $G_{\alpha}$ -peptide hotspots, we predicted GPCR hotspot swapping mutations to allow promiscuous coupling of  $\beta_2AR$  to  $G_{\alpha_q}$ . We observed that the residues Q384(s-pep)/L349(q-pep) (H5.16) make sustained interactions with Q229<sup>5.68</sup> ( $\beta_2AR$ )/W244<sup>5.66</sup> ( $V_{1A}R$ ), respectively (Fig. 4 *B, i* and *ii*). Although Q384(s-pep)/L349(q-pep) interact with residues on TM5 in both  $\beta_2AR$  and  $V_{1A}R$ , the hydrophilic interaction pair in  $\beta_2AR$ :s-pep is swapped to a hydrophobic interaction pair in  $V_{1A}R$ :q-pep (Fig. 4 *B, i* and *ii*), suggesting that this interaction pair could be a selectivity filter. To further strengthen the binding and coupling of  $G_{\alpha_q}$  to  $\beta_2AR$  in the TM5 region, we proposed the double mutant R228I<sup>5.67</sup>–Q229W<sup>5.68</sup>. The C terminus residue E392<sup>H5.24</sup> orients the s-pep toward the basic residue patch K270<sup>6.33</sup>, R328<sup>7.55</sup>, and R333<sup>8.51</sup> located between TM6 and TM7. The E355<sup>H5.22</sup> residue in q-pep orients the C terminus toward ICL1/TM2, interacting with R81<sup>ICL1</sup>, K82<sup>ICL1</sup>, T83<sup>ICL1</sup>, S84<sup>2.37</sup>, and R85<sup>2.38</sup> in  $V_{1A}R$ . From the MD simulation analysis, we observe that the dynamics of noncognate  $\beta_2AR$ :q-pep complex samples a finite but small population of the conformation similar to that of the cognate  $V_{1A}R$ :q-pep interaction. This guides

our hypothesis that GPCRs may couple to different  $G_{\alpha}$  proteins with different interfaces, but the interfaces for the noncognate  $G$  proteins could be latent cavities with weak interactions. We predicted that mutations of the  $\beta_2AR$  TM5 interface that mimic  $V_{1A}R$  may stabilize the short-lived  $V_{1A}R$ :q-pep-like orientation observed in  $\beta_2AR$ :q-pep. We expressed and tested a  $\beta_2AR$ –R228I<sup>5.67</sup>–Q229W<sup>5.68</sup> ( $\beta_2AR$ -DM) construct which produced an IP-1 signal about threefold greater than WT  $\beta_2AR$  (Fig. 5 *A, Left*). We also measured cAMP activity from the double-mutant construct, which showed a nonsignificant reduction in the  $G_{\alpha_s}$  pathway activity (Fig. 5 *A, Right*). This result suggests that the  $\beta_2AR$ -DM does complex with  $G_{\alpha_q}$  protein, and also with  $G_{\alpha_s}$  but with less coupling strength.

MD simulations of the q-pep bound to  $\beta_2AR$ -DM:q-pep were started from a  $G_{\alpha_q}$ -like and  $G_{\alpha_s}$ -like orientation. Results show favorable interaction in the  $G_{\alpha_q}$ -like orientation (Fig. 4 *B, iii*), with E355<sup>H5.22</sup> of q-pep stably binding to Q142<sup>34.54</sup> in  $\beta_2AR$ -DM. We predicted that a third mutation of Q142<sup>34.54</sup> to lysine in  $\beta_2AR$ -DM would further strengthen the q-pep interaction with  $\beta_2AR$  in  $G_{\alpha_q}$ -like orientation. As predicted, the triple mutant  $\beta_2AR$ –Q142K<sup>34.54</sup>–R228I<sup>5.67</sup>–Q229W<sup>5.68</sup> simulations showed q-pep binding in a similar interface to q-pep in  $V_{1A}R$ :q-pep (Fig. 4 *B, iv*). Agonist-induced IP-1 production significantly increased in the triple mutant compared with WT  $\beta_2AR$  (Fig. 5 *A, Left*). Measurement of agonist-induced cAMP showed a significant reduction in the triple mutant compared with WT  $\beta_2AR$  (Fig. 5 *A, Right*). We

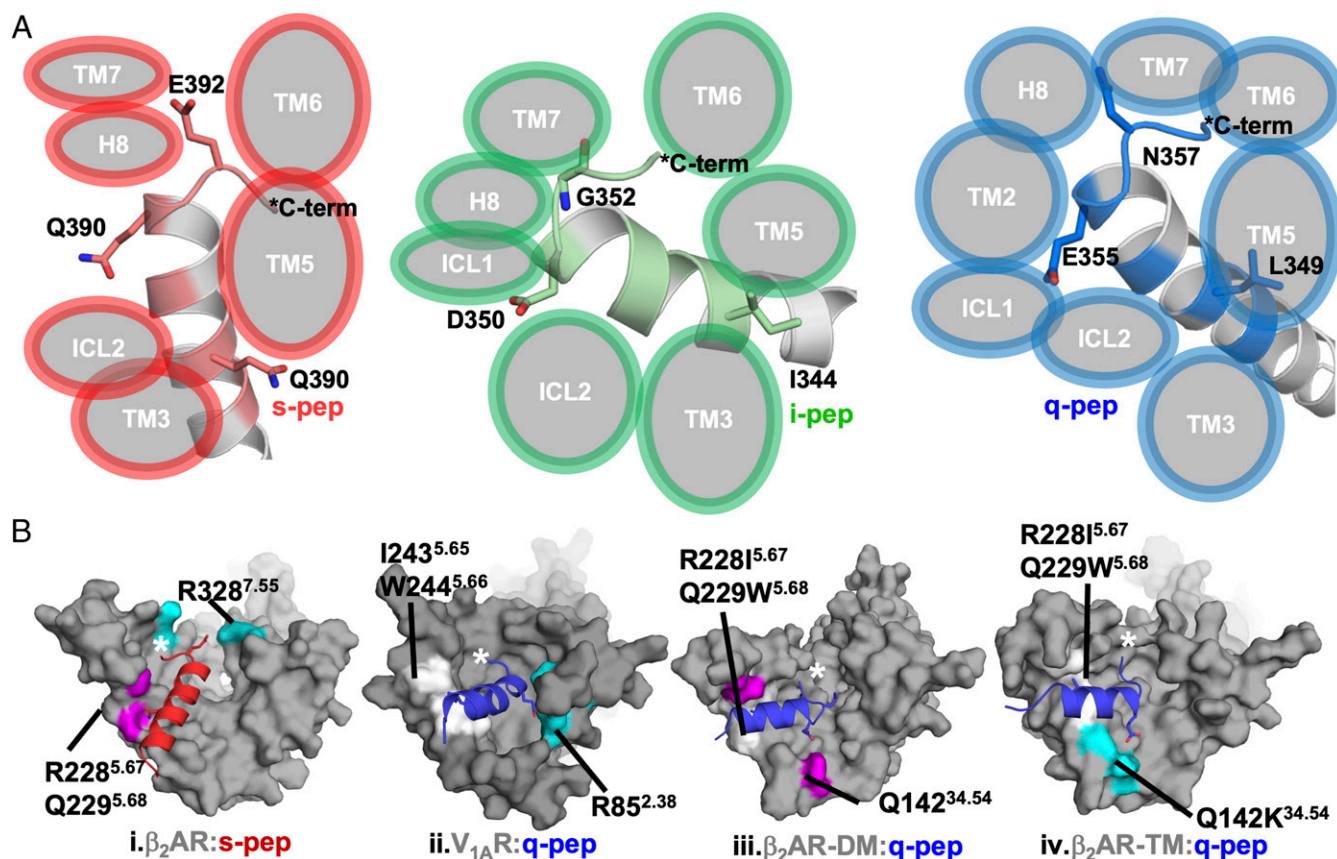


**Fig. 4.** Reshaping of the IC surface of  $\beta_2AR$  to accommodate  $G_{\alpha_q}$ . (A) The regions in the IC surface of the GPCR that interact with their respective cognate  $G$  peptides, as calculated from the MD simulation trajectories. The size of the circles shows the level of interaction with that particular TM helix. The larger the circle, the more favorable and stronger is the interaction with the receptor. The s-pep interaction with IC region of  $\beta_2AR$  is shown in red, i-pep interaction with the CB<sub>1</sub>R is shown in green, and q-pep interaction with  $V_{1A}R$  is shown in blue. The peptides are shown in cartoon representation. The C termini of the  $G_{\alpha}$  peptides are indicated by an asterisk in the figure. (B) (i) The orientation of binding of the s-pep (red cartoon) in  $\beta_2AR$ . Residues R228<sup>5.67</sup> and Q229<sup>5.68</sup> anchor H5.16 of s-pep to TM5, while R328<sup>7.55</sup> draws the C terminus (H5.24) toward TM6 and TM7. (ii) The corresponding q-pep (blue cartoon) H5.16 anchoring residues in TM5 are W244<sup>5.66</sup> and I243<sup>5.65</sup> in  $V_{1A}R$ , and the R85<sup>2.38</sup> residue draws the C terminus (H5.22) of q-pep toward ICL1 and TM2. (iii) The q-pep orientation in the double-mutant  $\beta_2AR$ –R228I–Q229W. (iv) The q-pep-bound triple-mutant  $\beta_2AR$ –Q142K–R228I–Q229W shows the same orientation as the q-pep in  $V_{1A}R$ .

tested whether  $G_{\alpha_i}$  signaling played a role in this decreased cAMP activity, but assays suggest this effect is insensitive to pertussis toxin (*SI Appendix, Fig. S3C*). Additionally, the dynamics of the triple mutant  $\beta_2AR:s\text{-pep}$  does not show lowering in  $s\text{-pep}$  binding (*SI Appendix, Fig. S4D*). We observe E225<sup>5,64</sup> in the triple-mutant  $\beta_2AR$  complementing the Q384<sup>H5,16</sup>, and the E392<sup>H5,24</sup> hotspot shows orientation to the TM6/TM7 region where it maintains contact with K270<sup>6,32</sup>, R328<sup>7,55</sup>, and R333<sup>8,51</sup>. Dose-response curves reveal how the triple mutation in  $\beta_2AR$  affects the potency and efficacy for the  $G_{\alpha_q}$  and  $G_{\alpha_s}$  interactions. For the  $G_{\alpha_q}$  pathway, we observe a reduction in the  $EC_{50}$  of isoproterenol from 2.97  $\mu M$  to 17.00 nM in the production of IP-1 by the  $\beta_2AR$  triple mutant, and approximately fourfold increase in overall efficacy (Fig. 5 *B, Left*). In the  $G_{\alpha_s}$  pathway, the  $EC_{50}$  of isoproterenol for cAMP production increased from 0.28 nM in the WT to 55.13 nM in the triple mutant, with approximately threefold reduction in overall efficacy (Fig. 5 *B, Right*).

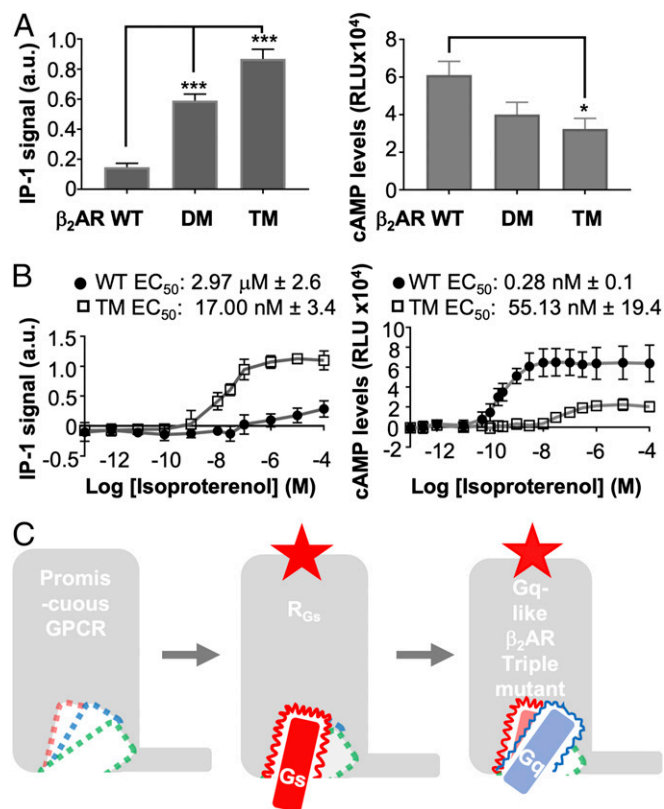


**Fig. 5.** Tuning the  $G_{\alpha_q}$  latent cavity in  $\beta_2AR$  generates a promiscuous signaling receptor. (A) Secondary messengers IP-1 and cAMP production in cells showing that the triple-mutant  $\beta_2AR$ -Q142K-R228I-Q229W and double-mutant  $\beta_2AR$ -R228I-Q229W efficiently couples to both  $G_{\alpha_q}$  and  $G_{\alpha_s}$  in the cell. Significance is denoted as \* $P < 0.05$ , \*\*\* $P < 0.001$ . (B) Dose-response curves for WT  $\beta_2AR$  and triple mutant ( $\beta_2AR$ -Q142K-R228I-Q229W) denoted as TM in this figure for brevity. IP-1 dose response curve for WT (circle markers) vs. triple mutant (square markers).  $EC_{50}$  values were calculated for each replicate ( $n = 3$ ) and the mean values for IP-1  $EC_{50} \pm SEM$  are reported on the graph for WT (circles; mean  $EC_{50}$ : 2.97  $\mu M \pm 2.6$ ) and triple mutant (squares; mean  $EC_{50}$ : 17.00 nM  $\pm 3.4$ ). cAMP dose-response curve for WT (circles) vs. triple mutant (squares).  $EC_{50}$  values were calculated for each replicate ( $n = 4$ ) and the mean values for cAMP  $EC_{50} \pm SEM$  are reported on the graph for WT (circles; mean  $EC_{50}$ : 0.28 nM  $\pm 0.1$ ) and triple mutant (squares; mean  $EC_{50}$ : 55.13 nM  $\pm 19.4$ ). (C) Model showing that GPCRs have latent cavities to fit  $G_{\alpha_s}$ ,  $G_{\alpha_i}$  and  $G_{\alpha_q}$  proteins. A  $G_{\alpha_s}$ -coupled receptor shows a deep attractive binding cavity for  $s\text{-pep}$ , while the latent binding cavities of  $G_{\alpha_q}$  and  $G_{\alpha_i}$  are shallow. Engineering the appropriate mutations, predicted from MD simulations, reshapes the IC surface in triple-mutant  $\beta_2AR$ , making it promiscuous to  $G_{\alpha_s}$ ,  $G_{\alpha_i}$ , and  $G_{\alpha_q}$ .

We summarize the results from these data in a model (Fig. 5C). We propose that GPCRs have latent cavities within their IC surface to bind different G proteins. The cavity in which the cognate G protein binds is attractive, with enthalpically favorable hotspots that lower the entropy of the complex and stabilize the agonist-bound GPCR interaction with the cognate G protein. Although GPCRs possess latent cavities for noncognate G proteins, the cavities are dynamic and unable to stabilize the noncognate G proteins, since they lack affinity. Promiscuous GPCRs have hotspot residues in the respective G-protein binding cavities that make them attractive to multiple G proteins. We note that possible selectivity hotspots outside of the  $G_{\alpha}$ -protein C terminus have not been probed in this study.

**Dynamic Reshaping of the IC Cavity in  $\beta_2AR$ .** MD results suggest that the triple-mutant undergoes dynamic reshaping of the IC cavity to bind both  $G_{\alpha_s}$  and  $G_{\alpha_q}$  proteins. MD simulations of the triple-mutant  $\beta_2AR$  coupled to  $s\text{-pep}$  and  $q\text{-pep}$  started from both  $G_{\alpha_s}$ -like and  $G_{\alpha_q}$ -like orientations revealed  $s\text{-pep}$  only binds in the  $G_{\alpha_s}$ -like cavity, and  $q\text{-pep}$  only binds in the  $G_{\alpha_q}$ -like cavity (Fig. 6 *A, i* and *ii*). The  $G_{\alpha_s}$ -interacting hotspots are shown as salmon-colored surface and span TM5, TM6, and TM7 and helix 8, with strongest interacting residues shown as spheres (Fig. 6 *A, i*). The residues that make contact with the  $q\text{-pep}$  are shown in blue surface, with the strongest interacting positions shown as blue spheres (Fig. 6 *A, ii*). The  $G_{\alpha_q}$ -interacting residues projected on the IC surface of  $s\text{-pep}$ -bound WT  $\beta_2AR$  show that  $G_{\alpha_q}$ -interacting residues are spread out and form a dispersed cavity when  $G_{\alpha_s}$  is bound (Fig. 6 *A, iii*). In the triple-mutant, the IC surface reshapes and positions the  $G_{\alpha_q}$ -interacting residues into a trident-like pattern spanning the IC portions of TM3, TM5, and TM6 and ICL1 and ICL2 (Fig. 6 *A, iv*). We projected this dynamic cavity on the interresidue distances between TM3 and TM6 and between TM3 and TM7, and we observe that WT  $\beta_2AR:q\text{-pep}$  samples a  $\beta_2AR$  cavity similar to the  $G_{\alpha_s}$ -bound crystal structure. This suggests that the lack of  $q\text{-pep}$  stabilizing hotspots prevents the stabilization of the  $\beta_2AR$  conformation observed in the triple-mutant complex with  $q\text{-pep}$  (Fig. 6 *B, Left*). The  $q\text{-pep}$  interaction in the triple mutant shows a very distinct conformation, with a narrower cavity between TM3 and TM6 and a slightly wider cavity between TM3 and TM7. This shrinking of the TM3 to TM6 distance is similar to that observed in the interaction of WT  $\beta_2AR$  with the  $G_{\alpha_i}$  protein in previous MD simulations (51). The  $\beta_2AR$  conformation sampled by the triple mutant with  $s\text{-pep}$  is similar to that sampled by WT  $\beta_2AR:s\text{-pep}$  (Fig. 2*B*), but the most populated conformational cluster shifts to a smaller TM3 to TM7 distance compared with WT  $\beta_2AR$ .

## Discussion

The 3D structures of GPCR–G-protein complexes predominantly inform us on how cognate G proteins interact with GPCRs in the nucleotide-free state. The dynamics of the agonist-bound GPCR has been well characterized by spectroscopic and computational studies (30–32, 52–55). However, the dynamics of the GPCRs with their cognate and, especially, noncognate G proteins is poorly understood, despite their relevance in cellular conditions (1, 5). Our study combining MD simulations and FRET sensor measurements has yielded the following conceptual advancements: 1) Agonist-bound and G-protein-bound GPCRs contain multiple latent IC cavities, which were not formerly characterized. The cognate and noncognate G proteins interact dynamically with their latent cavities with varying strengths. 2) The C terminus of  $G_{\alpha_s}$ ,  $G_{\alpha_i}$ , and  $G_{\alpha_q}$  proteins assume a small ensemble of unique orientations when coupled to their cognate GPCRs. This ensemble explains the variations observed in the coupling strengths of the same G protein to different GPCRs. 3) Engineering the latent cavities with hotspots



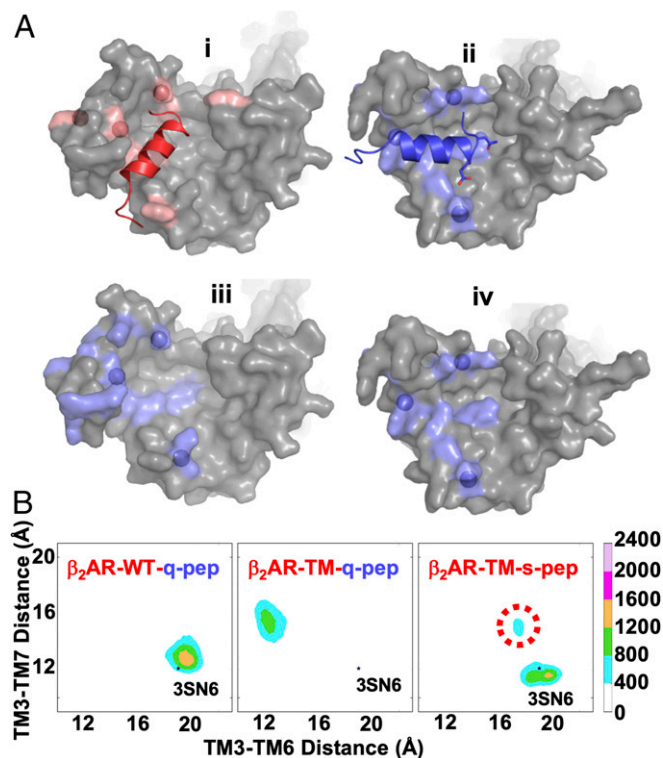


**Fig. 6.** Dynamic reshaping of the  $G\alpha_q$  cavity in a  $G\alpha_s$ -coupled receptor mutant: making  $\beta_2$ AR promiscuous toward  $G\alpha_q$  and  $G\alpha_s$ . (A) (i) The IC surface rendering of WT  $\beta_2$ AR with the residues involved in binding of s-pep shown in red surface. The bright red spheres are the residues that interact strongly with the s-pep. (ii) MD simulations of the triple-mutant  $\beta_2$ AR-Q142K-R228I-Q229W (denoted as  $\beta_2$ AR-TM in the figure for brevity) shows formation of a favorable  $G\alpha_q$ -like cavity with q-peptide wedged. (iii) This is the surface of the residues shown in (ii) when projected on the IC surface of WT  $\beta_2$ AR. This surface shows that the residues that should form a favorable cavity for  $G\alpha_q$  are spread out in the WT  $\beta_2$ AR. (iv) MD simulations of the double mutant of  $\beta_2$ AR show reshaping of these residues in (iii) to form a "trident"-like pattern. These are representative snapshots taken from the most populated conformation cluster from the MD simulations. (B) Ensemble of conformations from MD simulations projected on the interresidue distances between TM3 and TM6 (distance between C $\alpha$  atoms of residues 3.50 and 6.30) and between TM3 and TM7 (distance between C $\alpha$  atoms of 7.53 and 3.50) for WT  $\beta_2$ AR with q-pep (Left),  $\beta_2$ AR triple mutant with q-pep (Center), and  $\beta_2$ AR triple mutant with s-pep (Right).

to the noncognate G proteins tunes the promiscuity of the GPCR. Using the hotspot residues identified for coupling of  $G\alpha_s$ ,  $G\alpha_i$ , and  $G\alpha_q$  proteins to their respective cognate GPCRs, we have tuned a latent  $G\alpha_q$ -binding cavity in  $\beta_2$ AR to additionally bind and signal through  $G\alpha_q$ . This promiscuous triple mutant  $\beta_2$ AR demonstrates the tunability of G-protein selectivity in GPCRs.

G-protein selectivity likely arises from 1) several kinetic steps involved in going from engaging the G protein in the GDP-bound state and transitioning to the nucleotide-free state and 2) the relative thermodynamic stabilities of various conformational states involved in these kinetic steps (56). Our study probes the relative thermodynamic stabilities of the agonist-GPCR- $G\alpha$ -peptide complexes for the cognate and noncognate  $G\alpha$  peptides in the presence of the same agonist. Previous studies showed that agonist binding results in increased conformational heterogeneity (30–32, 57) in  $\beta_2$ AR (R+Ag; Fig. 7B). Pushing this further, our study shows that G-protein insertion, be it cognate or noncognate, leads to dynamic conformational heterogeneity in the GPCR IC cavity (R+Ag+G) and to a moderate entropic stabilization (Fig. 7B). Importantly, the GPCR cytosolic pocket continues to exhibit

a high degree of structural plasticity, and the cognate G protein reduces the entropy of residues in the GPCR cavity (Fig. 2A), stabilizing the receptor and enabling it to clamp down on the  $G\alpha$  C terminus (SI Appendix, Fig. S2B). The presence of enthalpically favorable intermolecular contacts between the cognate G protein and its preferred cavity leads to full complexation and productive signaling (Fig. 7A, iii and Fig. 7B). In contrast, the weak interactions between the GPCR cavity and noncognate G proteins result in the dissociation of  $G\alpha$  C terminus without productive complexation and signaling (Fig. 7A, iv). Incorporation of single G-protein-selective residues in the latent cavities, whether by evolution or engineering, is sufficient to reshape the GPCR IC surface for productive coupling with the noncognate G proteins. We hypothesize that promiscuously coupling GPCRs evolved to make these latent cavities highly attractive, while selective GPCRs are under evolutionary pressure to optimize the affinity between one cognate G protein and cavity.

One of the caveats of this study is our focus on only the C terminus of the G protein. The  $G\alpha$  C terminus is a known determinant of G-protein selectivity, and it has long been established that swapping the last three amino acids between the  $G\alpha_i$  and  $G\alpha_q$  isoforms is sufficient to confer promiscuous signaling from chimeric G proteins in HEK293 cells (28). Our focus on GPCR- $G\alpha$  C terminus interactions prevents confounding effects from the integration of signaling downstream of endogenous and chimeric G proteins. Nonetheless, we acknowledge that other regions are likely involved in G-protein selectivity. Another caveat is that many of our MD simulations were started from a homology model of the receptor- $G\alpha$ -peptide complex. The accuracy of our dynamics and hotspot predictions will be enhanced as more structures of the GPCR-G-protein complexes emerge in literature.

This study fills the knowledge gap in linking the dynamics of ligand-GPCR complexes to the dynamics of G-protein coupling and provides a framework to interpret variance in the strength of interaction between different GPCRs and G proteins.

## Materials and Methods

**Modeling of the GPCRs and Agonists.** The summarized modeling details are given in SI Appendix, Table S1. Structures of the GPCRs studied were modeled based on homology to either  $\beta_2$ AR,  $\mu$ OR, or CB $_1$ R templates. The models were then aligned to the active states of  $\beta_2$ AR or Rhodopsin in the 3SN6 and 4J4Q PDB structures.  $G\alpha$  peptides were modeled using the  $\alpha 5$  helix of  $G\alpha_s$  in 3SN6, and then aligned to the  $\alpha 5$  helix of  $G\alpha_i$  or transducin in 3SN6 and 4J4Q. Structures were minimized using the MacroModel [Schrödinger Release 2015-4; MacroModel (2015); Schrödinger, LLC] application before simulation with Groningen Machine for Chemical Simulations (GROMACS). For more details, please see SI Appendix.

**Details of MD Simulations.** MD simulations were performed in explicit POPC lipid bilayer and water using gromos 53a6 force field and following a standard protocol for GPCRs used in our laboratory (29). Details are in SI Appendix.

**Computational Data Analysis.** One-microsecond ensemble trajectories were used for analyzing intermolecular contacts and interaction energies for GPCR-peptide pairs. Individual energies were calculated for each amino acid of the  $G\alpha$  peptides with the entire GPCR using the GROMACS "energy" application. The total nonbond energy from short-range (within 12 Å) coulombic and van der Waals forces was extracted from an energy log file and summed for the total nonbond interaction energy.  $G\alpha$ -peptide residues showing above-average interaction energy (Fig. 3A) are considered critical residues and potential "hotspots." Intermolecular contacts were calculated in Visual Molecular Dynamics (VMD) using Tcl scripts to identify the frequency of pairwise interactions within 5 Å between peptides and receptors. Contacts made with greater than or equal to 50% frequency were deemed critical contacts. Peptide residues deemed "critical" from both interaction energy and intermolecular contact analysis were strongly considered for their role as "hotspots" for G-protein selectivity.



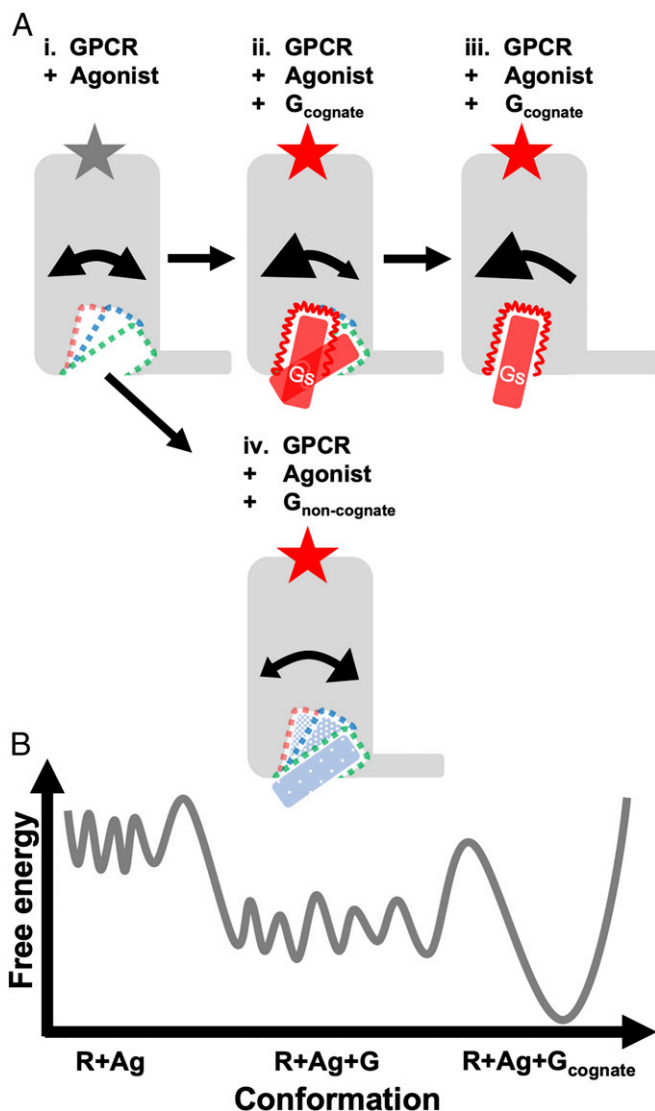


**Fig. 7.** The Goldilocks Effect: Cognate peptides fit “just right” for productive activation and signaling. (A) A model of the dynamics of the GPCR IC cavity and the C terminus of the  $G\alpha$  proteins, cognate and noncognate, complexed with an agonist-bound GPCR. Double-sided curved arrows are drawn to show (i) balanced dynamic movement of GPCR TM bundle and  $G\alpha$  C terminus between the dominant and latent cavities in the IC interface during the apo state, (ii) or skewed toward the dominant cavity upon initial complexation with cognate G protein, and (iv) skewed to the latent cavity upon complexing with a noncognate G protein. (iii) Strong, unidirectional arrows reveal stabilization of the dominant cavity during G-protein activation. (B) Schematic free-energy landscape describes the relative stability of the GPCR during agonist binding, transient interaction with G proteins, and full complexation with a cognate G protein.

**Calculation of first-order torsional entropy.** The first-order torsional entropy of the G-protein interacting residues shown in Fig. 2A was calculated using methods developed in-house (30). Further details of this analysis can be found in [SI Appendix](#).

**Calculation of the insertion angles of the G protein.** We measured the angle between the principal axis of the helical portion of the G $\alpha$  peptide (H5.13-H5.23) and the principal axis of the GPCR TM bundle, for each frame of the trajectory. The angle  $\theta$  was calculated from the dot product of these vectors using  $a \cdot b = \|a\| \|b\| \cos \theta$ .

**Calculation of GPCR IC cavity width and active-state complex metrics.** To measure the conformational flexibility in the IC cavity of the receptor, we measured the distance between C $\alpha$  atoms of the residues 3.50 and 6.30 for each receptor (numbers shown using Ballesteros–Weinstein numbering system). The distance

between the residues in this pair is used as a standard indicator of receptor activation state (46). We also measured the distance between the C $\alpha$  atoms of the residues 3.50 and 7.53 as another indication of receptor activation state.

**Conformational clustering method.** RMSD clustering in coordinates was used to determine the number of conformational clusters sampled by G $\alpha$  peptides within the 1- $\mu$ s ensemble of simulations. C $\alpha$  atoms from the GPCR TMs were aligned for the least-squares fit to serve as a frame of reference for comparing peptide orientations based on the backbone atoms of G $\alpha$ -peptide positions H5.12 to H5.26. The aligned G $\alpha$ -peptide conformations were clustered using the “gromos” method in the GROMACS “cluster” application, with a cutoff of 2 Å (58). This procedure identifies the centroid with the largest number of neighboring structures within the cutoff distance and sorts them to a unique cluster, repeating the same procedure with the remaining, unsorted structures.

**Statistical analysis.** The mean  $\pm$  SEM was determined from each of five 200-ns replicates of the 1- $\mu$ s ensemble trajectory. Means were compared using one-way ANOVA followed by Tukey's posttest to assess significance for multiple comparisons, using GraphPad Prism version 7.00 for Windows (GraphPad Software, <https://www.graphpad.com>) (Fig. 2A and *SI Appendix, Fig. S4A*). The Kolmogorov–Smirnov test statistic was calculated for each distribution of GPCR IC cavity width (TM3 to TM6 distances), to compare the variance of each distribution (59). The sample size of the distribution was calculated as 50,000 frames. Each comparison rejected the null hypothesis, and *P* values were too small to be calculated, due to limitations of machine precision (limited to  $2.2 \times 10^{-16}$ ), but all *P* values for each comparison were significantly less than  $1.0 \times 10^{-4}$  (*SI Appendix, Fig. S2B and Table S3*).

## Experimental Methods

Experiments were conducted similarly to procedures outlined in our previous study (29). Details of "Reagents and buffers," "Molecular cloning," and "Mammalian cell preparation and sensor expression" are found in *SI Appendix*.

**cAMP Assays.** HEK293T-Flip-in cells were transiently transfected (XtremeGENE HP) according to manufacturer's instructions. Where indicated, 10 h after transfection, cells were incubated with 100 ng·mL<sup>-1</sup> pertussis toxin (PTX) for 20 h. Between 28 h and 32 h posttransfection, (XtremeGENE HP) HEK293T cells expressing indicated sensor were harvested to assess cAMP levels using the bioluminescent cAMP Glo assay (Promega). Cells were gently suspended in their original media, were counted using a hemocytometer, and were spun down (350 × g, 3 min). Cells were resuspended in an appropriate volume of PBS (pH 7.4; Gibco) supplemented with 800 μM ascorbic acid and 0.2% dextrose (wt/vol) to reach 4 × 10<sup>6</sup> cells/mL density. Cell suspensions were aliquoted into 384-well opaque plates. To assess Emax for cAMP production, cells were incubated with 100 μM of isoproterenol for 15 min at 37 °C. For dose-response curves, cells were incubated under the same conditions with a range of isoproterenol concentrations from 100 fM to 100 μM. Subsequently, cells were lysed and the protocol was followed according to the manufacturer's recommendation (Promega). Luminescence was measured using a microplate luminometer reader (SpectraMax M5e; Molecular Devices). The cAMP levels (relative luminescence unit) were evaluated by subtracting the isoproterenol conditions from the untreated conditions. Each experiment had four technical repeats per condition and was independently repeated at least three times (*n* > 3). To obtain EC<sub>50</sub> and Emax, dose-response data were fit to a sigmoidal dose-response equation using nonlinear least-squares regression.

**IP-1 Assays.** At 28 h to 32 h posttransfection, (XtremeGENE HP) HEK293T cells expressing the indicated sensor were harvested to assess IP-1 levels using the IP-One HTRF assay kit (Cisbio). Cells were gently suspended in their original media, counted using a hemocytometer, and spun down (350 × g, 3 min). An appropriate volume of StimB buffer (CisBio: 10 mM Hepes, 1 mM CaCl<sub>2</sub>, 0.5 mM MgCl<sub>2</sub>, 4.2 mM KCl, 146 mM NaCl, 5.5 mM glucose, 50 mM LiCl, pH 7.4) was added to reach 3 × 10<sup>6</sup> cells/mL density. Cells were incubated with 100 μM isoproterenol at 37 °C for 120 min. For dose-response curves, cells were incubated under the same conditions with a range of isoproterenol concentrations from 100 fM to 100 μM. Following the manufacturer's protocol, each reaction suspension was then incubated for 1 h shaking (500 rpm) at room temperature with 15 μL of IP-1 conjugated to d2 dye and 15 μL of terbium cryptate-labeled anti-IP-1 monoclonal antibody prepared and stored as recommended by the manufacturer. IP-1 FRET spectra were collected by exciting samples at 340 nm (band-pass 15 nm). Emission counts were recorded from 600 nm to 700 nm (band-pass 10 nm) using a long-pass 475-nm filter (FSQ GG475; Newport). Raw IP-1 signal was calculated from the 665 nm to 620 nm ratio. Data are presented as a change in raw IP-1 ratio following drug treatment. Each experiment had four repeats per condition and was independently repeated at least three times (*n* > 3). To obtain EC<sub>50</sub> and Emax, dose-response

data were fit to a sigmoidal dose–response equation using nonlinear least-squares regression. Compared with the cAMP data, the IP-1 data were better explained by fitting to a dose–response model ( $\Sigma \text{Residuals}^2 = 0.01$ ) than by fitting to a linear model ( $\Sigma \text{Residuals}^2 = 0.05$ ).

**Statistical Analysis.** Data are expressed as mean values  $\pm$  SEM. Experiments were independently conducted at least three times, with three to six technical repeats per condition ( $n > 3$ ). Statistical analysis was performed using GraphPad Prism 7.0c (GraphPad Software, Inc.). Statistical significance was performed for individual experiments using paired Student's *t* test. To assess

how the data varied across experimental repeats, data were pooled, and paired or unpaired Student's *t* tests were conducted to evaluate significance. One-way ANOVA with a Tukey's posttest was performed to assess significance when evaluating comparisons between multiple conditions (Figs. 3B and 5A) with *P* values  $*P \leq 0.05$ ;  $**P \leq 0.01$ ;  $***P \leq 0.001$ ; and  $****P \leq 0.0001$ .

**ACKNOWLEDGMENTS.** Research in this publication is supported by Grant NIH-R01GM117923 (to N.V. and S.S.) and Maximizing Investigator Research Award Grant NIH-R35GM126940 (to S.S.).

1. I. Masuho *et al.*, Distinct profiles of functional discrimination among G proteins determine the actions of G protein-coupled receptors. *Sci. Signal.* **8**, ra123 (2015).
2. Y. Namkung *et al.*, Functional selectivity profiling of the angiotensin II type 1 receptor using pathway-wide BRET signaling sensors. *Sci. Signal.* **11**, eaat1631 (2018).
3. F. Mende *et al.*, Translating biased signaling in the ghrelin receptor system into differential in vivo functions. *Proc. Natl. Acad. Sci. U.S.A.* **115**, E10255–E10264 (2018).
4. Y. Namkung *et al.*, Quantifying biased signaling in GPCRs using BRET-based biosensors. *Methods* **92**, 5–10 (2016).
5. R. R. Neubig, Membrane organization in G-protein mechanisms. *FASEB J.* **8**, 939–946 (1994).
6. K. Wenzel-Seifert, R. Seifert, Molecular analysis of  $\beta_2$ -adrenoceptor coupling to  $G_s$ ,  $G_i$ , and  $G_q$  proteins. *Mol. Pharmacol.* **58**, 954–966 (2000).
7. W. Stallaert, J. F. Dorn, E. van der Westhuizen, M. Audet, M. Bouvier, Impedance responses reveal  $\beta_2$ -adrenergic receptor signaling pluridimensionality and allow classification of ligands with distinct signaling profiles. *PLoS One* **7**, e29420 (2012).
8. L. Zhou *et al.*, Functional selectivity of GPCR signaling in animals. *J. Biol. Chem.* **109**, 7809–7820 (2016).
9. L.-P. Picard, A. M. Schönege, M. J. Lohse, M. Bouvier, Bioluminescence resonance energy transfer-based biosensors allow monitoring of ligand- and transducer-mediated GPCR conformational changes. *Commun. Biol.* **1**, 106 (2018).
10. S. G. F. Rasmussen *et al.*, Crystal structure of the  $\beta_2$  adrenergic receptor-Gs protein complex. *Nature* **477**, 549–555 (2011).
11. B. Carpenter, R. Nehmé, T. Warne, A. G. W. Leslie, C. G. Tate, Erratum: Structure of the adenosine  $A_{2A}$  receptor bound to an engineered G protein. *Nature* **538**, 542 (2016).
12. C. J. Draper-Joyce *et al.*, Structure of the adenosine-bound human adenosine  $A_1$  receptor-G<sub>i</sub> complex. *Nature* **558**, 559–563 (2018).
13. J. García-Nafria, R. Nehmé, P. C. Edwards, C. G. Tate, Cryo-EM structure of the serotonin 5-HT<sub>1B</sub> receptor coupled to heterotrimeric G<sub>o</sub>. *Nature* **558**, 620–623 (2018).
14. Y. Kang *et al.*, Cryo-EM structure of human rhodopsin bound to an inhibitory G protein. *Nature* **558**, 553–558 (2018).
15. A. Koehl *et al.*, Structure of the  $\mu$ -opioid receptor-G<sub>i</sub> protein complex. *Nature* **558**, 547–552 (2018).
16. K. Krishna Kumar *et al.*, Structure of a signaling cannabinoid receptor 1-G protein complex. *Cell* **176**, 448–458.e12 (2019).
17. T. Flock *et al.*, Universal allosteric mechanism for G $\alpha$  activation by GPCRs. *Nature* **524**, 173–179 (2015).
18. T. Flock *et al.*, Selectivity determinants of GPCR-G-protein binding. *Nature* **545**, 317–322 (2017).
19. S. K. Wong, E. M. Ross, Chimeric muscarinic cholinergic:beta-adrenergic receptors that are functionally promiscuous among G proteins. *J. Biol. Chem.* **269**, 18968–18976 (1994).
20. S. K. Wong, G protein selectivity is regulated by multiple intracellular regions of GPCRs. *Neurosignals* **12**, 1–12 (2003).
21. E. Kostenis, B. R. Conklin, J. Wess, Molecular basis of receptor/G protein coupling selectivity studied by coexpression of wild type and mutant m2 muscarinic receptors with mutant G $\alpha_q$  subunits. *Biochemistry* **36**, 1487–1495 (1997).
22. J. Wess, Molecular basis of receptor/G-protein-coupling selectivity. *Pharmacol. Ther.* **80**, 231–264 (1998).
23. J. Wess, M. R. Brann, T. I. Bonner, Identification of a small intracellular region of the muscarinic m3 receptor as a determinant of selective coupling to PI turnover. *FEBS Lett.* **258**, 133–136 (1989).
24. B. R. Conklin, Z. Farfel, K. D. Lustig, D. Julius, H. R. Bourne, Substitution of three amino acids switches receptor specificity of Gq  $\alpha$  to that of Gi  $\alpha$ . *Nature* **363**, 274–276 (1993).
25. E. Kostenis, M. Y. Degtyarev, B. R. Conklin, J. Wess, The N-terminal extension of Galpha is critical for constraining the selectivity of receptor coupling. *J. Biol. Chem.* **272**, 19107–19110 (1997).
26. C.-S. S. Yang, N. P. Skiba, M. R. Mazzoni, H. E. Hamm, Conformational changes at the carboxyl terminus of Galpha occur during G protein activation. *J. Biol. Chem.* **274**, 2379–2385 (1999).
27. N. Van Eps, W. M. Oldham, H. E. Hamm, W. L. Hubbell, Structural and dynamical changes in an  $\alpha$ -subunit of a heterotrimeric G protein along the activation pathway. *Proc. Natl. Acad. Sci. U.S.A.* **103**, 16194–16199 (2006).
28. A. I. Kaya *et al.*, A conserved phenylalanine as a relay between the  $\alpha 5$  helix and the GDP binding region of heterotrimeric Gi protein  $\alpha$  subunit. *J. Biol. Chem.* **289**, 24475–24487 (2014).
29. A. Semack, M. Sandhu, R. U. Malik, N. Vaidehi, S. Sivaramakrishnan, Structural elements in the G $\alpha$ s and G $\alpha_q$  C termini that mediate selective G protein-coupled receptor (GPCR) signaling. *J. Biol. Chem.* **291**, 17929–17940 (2016).
30. M. J. Niesen, S. Bhattacharya, N. Vaidehi, The role of conformational ensembles in ligand recognition in G-protein coupled receptors. *J. Am. Chem. Soc.* **133**, 13197–13204 (2011).
31. R. Nygaard *et al.*, The dynamic process of  $\beta_2$ -adrenergic receptor activation. *Cell* **152**, 532–542 (2013).
32. A. Manglik *et al.*, Structural insights into the dynamic process of  $\beta_2$ -adrenergic receptor signaling. *Cell* **161**, 1101–1111 (2015).
33. M. E. Maguire, P. M. Van Arsdale, A. G. Gilman, An agonist-specific effect of guanine nucleotides on binding to the beta adrenergic receptor. *Mol. Pharmacol.* **12**, 335–339 (1976).
34. B. T. DeVree *et al.*, Allosteric coupling from G protein to the agonist-binding pocket in GPCRs. *Nature* **535**, 182–186 (2016).
35. S. Lee, A. K. Nivedha, C. G. Tate, N. Vaidehi, Dynamic role of the G protein in stabilizing the active state of the adenosine  $A_{2A}$  receptor. *Structure* **27**, 703–712.e3 (2019).
36. S. Sivaramakrishnan, J. A. Spudich, Systematic control of protein interaction using a modular ERK  $\alpha$ -helix linker. *Proc. Natl. Acad. Sci. U.S.A.* **108**, 20467–20472 (2011).
37. R. U. Malik *et al.*, Detection of G protein-selective G protein-coupled receptor (GPCR) conformations in live cells. *J. Biol. Chem.* **288**, 17167–17178 (2013).
38. A. Semack, R. U. Malik, S. Sivaramakrishnan, G protein-selective GPCR conformations measured using FRET sensors in a live cell suspension fluorometer assay. *J. Vis. Exp.*, 115 e54696 (2016).
39. E. K. M. Johnstone, K. D. G. Pfeiffer, “Bioluminescence resonance energy transfer approaches to discover bias in GPCR signaling” in *G Protein-Coupled Receptors in Drug Discovery*, M. Filizola, Ed. (Springer, 2015), pp. 191–204.
40. M. Maziarz, M. Garcia-Marcos, Rapid kinetic BRET measurements to monitor G protein activation by GPCR and non-GPCR proteins. *Methods Cell Biol.* **142**, 145–157 (2017).
41. T. M. Gupte, R. U. Malik, R. F. Sommes, M. Ritt, S. Sivaramakrishnan, Priming GPCR signaling through the synergistic effect of two G proteins. *Proc. Natl. Acad. Sci. U.S.A.* **114**, 3756–3761 (2017).
42. T. Kenakin, Functional selectivity and biased receptor signaling. *J. Pharmacol. Exp. Ther.* **336**, 296–302 (2011).
43. R. K. Sunahara, J. J. Tesmer, A. G. Gilman, S. R. Sprang, Crystal structure of the adenylyl cyclase activator G<sub>ss</sub>. *Science* **278**, 1943–1947 (1997).
44. K. Y. Chung *et al.*, Conformational changes in the G protein Gs induced by the  $\beta_2$  adrenergic receptor. *Nature* **477**, 611–615 (2011).
45. K. Eichel, M. von Zastrow, Subcellular organization of GPCR signaling. *Trends Pharmacol. Sci.* **39**, 200–208 (2018).
46. D. L. Farrens, C. Altenbach, K. Yang, W. L. Hubbell, H. G. Khorana, Requirement of rigid-body motion of transmembrane helices for light activation of rhodopsin. *Science* **274**, 768–770 (1996).
47. J. A. Ballesteros, H. Weinstein, “Integrated methods for the construction of three-dimensional models and computational probing of structure-function relations in G protein-coupled receptors” in *Methods in Neurosciences*, S. C. Sealfon, Ed. (Academic, 1995), Vol. **25**, pp. 366–428.
48. D. M. Perez, M. B. DeYoung, R. M. Graham, Coupling of expressed  $\alpha 1B$ - and  $\alpha 1D$ -adrenergic receptor to multiple signaling pathways is both G protein and cell type specific. *Mol. Pharmacol.* **44**, 784–795 (1993).
49. C. Prioleau, I. Visiers, B. J. Ebersole, H. Weinstein, S. C. Sealfon, Conserved helix 7 tyrosine acts as a multistate conformational switch in the 5HT<sub>2C</sub> receptor. Identification of a novel “locked-on” phenotype and double revertant mutations. *J. Biol. Chem.* **277**, 36577–36584 (2002).
50. O. Fritze *et al.*, Role of the conserved NPxxY<sub>5,6F</sub> motif in the rhodopsin ground state and during activation. *Proc. Natl. Acad. Sci. U.S.A.* **100**, 2290–2295 (2003).
51. A. S. Rose *et al.*, Position of transmembrane helix 6 determines receptor G protein coupling specificity. *J. Am. Chem. Soc.* **136**, 11244–11247 (2014).
52. G. Swaminath *et al.*, Sequential binding of agonists to the  $\beta_2$  adrenoceptor. Kinetic evidence for intermediate conformational states. *J. Biol. Chem.* **279**, 686–691 (2004).
53. S. Bhattacharya, N. Vaidehi, Computational mapping of the conformational transitions in agonist selective pathways of a G-protein coupled receptor. *J. Am. Chem. Soc.* **132**, 5205–5214 (2010).
54. N. Vaidehi, T. Kenakin, The role of conformational ensembles of seven transmembrane receptors in functional selectivity. *Curr. Opin. Pharmacol.* **10**, 775–781 (2010).
55. T. H. Kim *et al.*, The role of ligands on the equilibria between functional states of a G protein-coupled receptor. *J. Am. Chem. Soc.* **135**, 9465–9474 (2013).
56. G. Gregorio *et al.*, Single-molecule analysis of ligand efficacy in  $\beta_2$ AR-G-protein activation. *Nature* **547**, 68–73 (2017).
57. S. Bhattacharya, N. Vaidehi, Differences in allosteric communication pipelines in the inactive and active states of a GPCR. *Biophys. J.* **107**, 422–434 (2014).
58. X. Daura *et al.*, Peptide folding: When simulation meets experiment. *Angew. Chem. Int. Ed.* **38**, 236–240 (1999).
59. F. Pedregosa *et al.*, Scikit-learn: Machine learning in Python. *J. Mach. Learn. Res.* **12**, 2825–2830 (2011).